RESEARCH PAPER

Nanoreactor-Enabled Formation of Graphitic Film from a Non-Graphitizing Precursor at Low-Temperature

Aliyeh Afzalalghom*, Ali Beitollahi, Seyed Mohammad Mirkazemi, Mahdi Maleki, Hossein Sarpoolaky

* *a_afzalalghom@metaleng.iust.ac.ir*

School of Metallurgy & Materials Engineering, Iran University of Science and Technology (IUST), Narmak, Tehran 16846, Iran

Received: December 2025 **Revised: January 2026** **Accepted: February 2026**
DOI: 10.22068/ijmse.4484

Abstract: *Graphite is produced by long-term heating of graphitizing precursors such as coke to 3000°C. However, most organic precursors are non-graphitizing, which cannot develop a graphite structure even at these super high temperatures. Gas-phase methods for graphite/graphene production, such as chemical vapor deposition (CVD), yield high-quality products but demand require catalysts, substrates, high-purity hydrocarbon gases, specialized furnaces, and temperatures exceeding 1000°C. Here, we demonstrate the synthesis of highly graphitized films with crystalline domains via low-temperature carbonization (900°C) of nanoporous polydivinylbenzene (PDVB) microspheres, without the need for a CVD system or catalysts. The films formed on the inner surface of the furnace quartz tube and were characterized by Raman spectroscopy, Fourier Transform Infrared (FTIR) spectroscopy, X-ray Diffraction (XRD), and high-resolution transmission electron microscopy (HRTEM). The Raman spectrum revealed a high degree of graphitization (I_{D_1})/I_G= 0.78), surpassing reported values for catalyst-free plasma- or low-pressure-assisted CVD. XRD showed a sharp diffraction peak at 2θ= 26.37° (d= 3.37 Å), exactly matching the diffraction peak of the (002) plane of Graphite-2H, while HRTEM and selected area electron diffraction confirmed crystalline domains with p63/mmc symmetry. We propose that the intricate network of nanopores(within PDVB microspheres serves as nanoreactors, enabeling) the generation and controlled release of fused benzene rings into the quartz tube, where they condense to form crystalline films. This approach reveals how a nanoscale confinement can be translated into a macroscopic, scalable route, offering a low-cost and facile method for graphite or graphene production.*

Keywords: *Nanoreactor, Graphite, Non-graphitizing, Catalyst-free, Nanoconfinement.*

1. INTRODUCTION

Graphite is composed of stacked layers of graphene held together by π–π interactions, exhibits high electron and ion conductivity. The sp^2 hybridization of carbon atoms xwithinx (in) the graphene layers also imparts high chemical and mechanical stability to this material. These properties, along with its low cost, have made graphite an (unrivalled) candidate for use as an anode in batteries and supercapacitors [1, 2]. The increasing demand for high-quality graphite in lithium batteries and supercapacitors, which is used in applications ranging from electronics to electric vehicles, and the controllability of synthetic graphite properties, have prompted researchers to develop novel, cost-effective, and scalable graphite production methods.

Synthetic graphite is typically made by high-temperature heat treatment of organic precursors which involves heating to ~3000°C for over 48 hours [3], which is both energy-intensive and costly. However, the more challenging issue of graphitization is the seriously limited choice of graphitizable precursors. Only a small group of organic compounds can form crystalline graphite [3-6], while most of them decompose into porous, disordered carbon [6]. Franklin [7] called the former graphitizing (Gr) precursors which include coal tar pitch, petroleum coke and the like, and the latter non-graphitizing (NGr) precursors involving synthetic or natural polymers like cellulose, chitin, polystyrene, and so on.

It is well known that synthesis from the gas phase typically leads to higher crystallinity compared to solid-state routes. Chemical vapor deposition (CVD) as a reliable gas phase method was utilized to produce highly crystalline graphite in 1994 [8]. However, following the discovery of graphene in 2001, this pathway was adopted to create few-layer or multilayer graphene [9]. The process involves charging high-purity hydrocarbon gases, such as methane, into a CVD furnace tube with multiple thermal zones, each equipped with a

[DOI: 10.22068/ijmse.4484]

metal catalyst layer copper or nickel on a Si/SiO_2 substrate. At temperatures above 1000°C, a thin layer of graphene forms. Although CVD leads to high quality graphene/graphite, but this method is associated with these challenges: i) complexity: the need for high-purity hydrocarbon and hydrogen gases, an accurate furnace with different thermal zones, procedure for removing catalyst layer and, transferring the graphene layer for the desired purpose, ii) impurity: from the dissolution of catalyst and substrate atoms in the produced layer, iii) high cost, and iv) limited size of final product: limited to the size of the substrate.

Recent research has focused on catalyst-free graphene synthesis to overcome some of the production challenges. Loung and colleagues [10] used joule heating of solid carbon precursors to produce graphene with turbostratic stacking. Kotbi et al [11]. synthesized graphene from ethylene gas via low-pressure plasma and flash heating on various substrates, but none produced highly crystalline graphene with low I_D/I_G ratios. Papale and co-workers [12] applied plasma-enhanced CVD to orange oil on silicon and quartz substrates, but did not achieve high crystallinity. Liu's team [13] used single-crystal Si wafers and carbon monoxide gas as the carbon source, but the graphitic structures only formed at temperatures higher than 1000°C. To the best of our knowledge, there is no report (of) a scalable gas-phase synthesis of graphene/graphite without using a catalyst, a CVD furnace with different thermal zones, pure hydrogen gas, and a substrate at a low temperature.

Divinylbenzene (DVB), composed of one benzene ring (a fundamental part of the graphene/graphite structure) and two vinyl arms, polymerizes to form a thermoset polymer, and if sulfonated in sulfuric acid, it yields 40% carbon material after carbonization to 1000°C [14], which is a high yield amongst polymers. Also, increasing the surface area of this polymer is easily achieved by employing aromatic and/or aliphatic hydrocarbons as porogens in the initial mixture [14].

Despite its promise, PDVB has generally failed to produce graphitic carbon. Asfaw and co-workers studied the carbonization of sulfonated polystyrene-co-poly(divinylbenzene) polyHIPEs to 1500°C [15], and no high degree of graphitization was obtained at such a high temperature. Even by employing iron as a strong catalyst, Liu and colleagues [14] could not develop (a) graphite structure to a high extent. Similar results were recorded for PDVB, poly(PDVB-co-vinylimidazole) [16], hyper crosslinked [17] or nitrogen-doped poly(St-DVB) [18] samples.

In our previous study [19], we demonstrated that nanopores in an NGr precursor sulfonated polydivinylbenzene (PDVB) microspheres can act as dynamic nanoreactors, enabling the local fusion of benzene rings resulting from the decomposition of pore walls and conversion to fused benzene rings (FBRs) followed by graphitic structure development inside pores at low temperature. However, that work was limited to microscale particles, and the broader implications of considering nanoreactors network the nanoporous intricate structure function for forming extended graphitic architectures out of microspheres remained unexplored. Here, we apply the nanoreactor concept to demonstrate the growth of graphitic films directly on the walls of a quartz tube at the low temperature of 900°C compared to 3000°C in graphitization and T >1000°C in CVD production method, without catalyst, substrate, or CVD processing. This approach reveals how a nanoscale confinement effect can be translated into a macroscopic, scalable route for graphitic film production. By bridging the gap between confined graphitization in microspheres and extended film growth, this work advances the importance of microstructure engineering for facilitating molecular self-assembly pathways instead of atomic carbon arrangement during graphite crystallization and provides a foundation for low-cost, scalable synthesis of graphitic materials.

2. EXPERIMENTAL PROCEDURES

2.1. Ingredients

Divinylbenzene monomer (DVB), α,α'-azobisiso-butyronitrile (AIBN) as an initiator, polyvinyl-pyrrolidone (PVP) as a stabilizer, hexadecyl trimethyl ammonium bromide (CTAB) as a surfactant, toluene and n-heptane as pore-generating agents (porogens), and concentrated sulfuric acid (95-97%) were all purchased from Merck.

2.2. Synthesis of Hierarchial Porous Carbon Microspheres

Porous PDVB microspheres were synthesized using a microsuspension polymerization method. The aqueous phase was prepared by dissolving 3.75 mg of polyvinylpyrrolidone (PVP) and 1.65 mg of cetyltrimethylammonium bromide (CTAB) in 50 mL of deionized water. The oil phase consisted of 2.5 mL toluene, 1.25 mL n-heptane, 6 mg of

[DOI: 10.22068/ijmse.4484]

azobisisobutyronitrile (AIBN) as the initiator, and 1 mL divinylbenzene (DVB) monomer. The aqueous and oil phases were emulsified at 12,000 rpm for 2 min using a Heidolph Silent Crusher homogenizer. Polymerization was then conducted in a three-neck flask under an argon atmosphere at 65°C for 6 hours. After completion, the reaction mixture was rapidly cooled to room temperature.

The polymer microspheres were collected by centrifugation at 9,000 rpm for 20 min. The precipitated microspheres were washed with a 50:50 (v/v) mixture of deionized water and ethanol to remove impurities. Finally, the washed white pellet was dried in a petri dish at 80°C for 24 hours in a Memmert dryer and labelled as PDVB.

2.3. Sulfonation

A two-neck Pyrex balloon equipped with a condenser was charged with 35 mL of concentrated sulfuric acid and heated to 80°C. Subsequently, 0.8 g of PDVB powder was added to the acid, forming a suspension that was stirred continuously at 100°C for 12 hours. During this period, the suspension's color changed from red to dark brown, indicating the progress of sulfonation. After 12 hours, the suspension was separated using a ceramic membrane filtration. The solid sulfonated PDVB was washed repeatedly with an excess amount of distilled water until the pH of the washing filtrate reached neutral (pH 7). Finally, the sulfonated PDVB was dried at 80°C for 24 hours in a Memmert oven.

2.4. Carbon Coating Formation via Carbonization

Sulfonated porous PDVB microspheres were carbonized to 900°C for 2 h with (a) heating rate of 2.5°C/min in a tubular furnace equipped with a quartz tube under a continuous argon gas flow. The quartz tube used (was) 1.5 m long and had an inner diameter of 2 cm. The furnace's hot zone spanned 20 cm in the center of the tube. The quartz tube was not cleaned between consecutive carbonization runs. Instead, a new PDVB sample was charged into the furnace, following the same heating profile to promote the deposition and reaction of decomposition products inside the tube. Over multiple cycles, a carbonaceous coating with a greyish luster accumulated on the interior walls of the quartz tube.

2.5. Characterization

This deposited matrix was carefully separated from the tube and designated GCNP (standing for graphitized coating from NGr polymer). The GCNP material was characterized using scanning electron microscopy (SEM), Fourier-transform infrared (FTIR) spectroscopy, Raman spectroscopy, X-ray diffraction (XRD), and high-resolution transmission electron microscopy (HRTEM).

SEM was conducted using a VEGA TESCAN scanning electron microscope at 20 KV. Prior to the analysis, the separated coatings from the quartz tube were sonicated in ethanol for 10 min. Fourier-transform infrared (FTIR) spectroscopy was performed using a PerkinElmer spectrometer with 2 cm^{-1} resolution in 400-4000 cm^{-1}. The Raman spectrum was recorded by a Raman spectrometer employing an Nd:YAG laser at 532 nm with (a) power of 90 mW. X-ray diffraction (XRD) patterns were collected on a Bruker D8 Advance X-ray diffractometer, using Cu Kα radiation with 0.04° resolution.

The graphitization degree was calculated by the Mering and Maire equation, and crystallite size was obtained by the Scherrer equation [20]:

Degree of graphitization from (the) Mering and Maire equation:

$$g = (0.3440 - d002)/(0.3440 - 0.3354)g \quad (1)$$

Crystallite size:

lateral crystallite size, $L_a = (k_1\lambda)/[\beta(100)\cos\theta(100)]L_a = (k_1\lambda)/[\beta(100)\cos\theta(100)]$ (2)

vertical crystallite size, $L_c = (k_2\lambda)/[\beta(002)\cos\theta(002)]L_c = (k_2\lambda)/[\beta(002\cos\theta(002)]$ (3)

Here, β is the peak half-height width, and k_1 and k_2 are 1.84 and 0.89, respectively.

High-resolution transmission electron microscopy (HRTEM) images and selected area electron diffraction (SAED) patterns were recorded on an FEI Tecnai G2 20F SuperTwin transmission electron microscope at 200 kV. Prior to imaging, samples were dispersed in ethanol by sonication and dropped onto copper grids. HRTEM data analysis was (performed) using the (Digital Micrograph) software (version 3.40.2804.0).

3. RESULTS AND DISCUSSION

The created carbon coating on the interior wall of the quartz tube as a result of repeatedly low-temperature carbonization of sulfonated PDVB (GCNP) was precisely separated from the tube and was characterized structurally and chemically without further processing.

3.1. Structural and Chemical Analysis of The Sample

Figure 1 shows images of the GCNP sample along with its Raman and FTIR spectra.

[DOI: 10.22068/ijmse.4484]

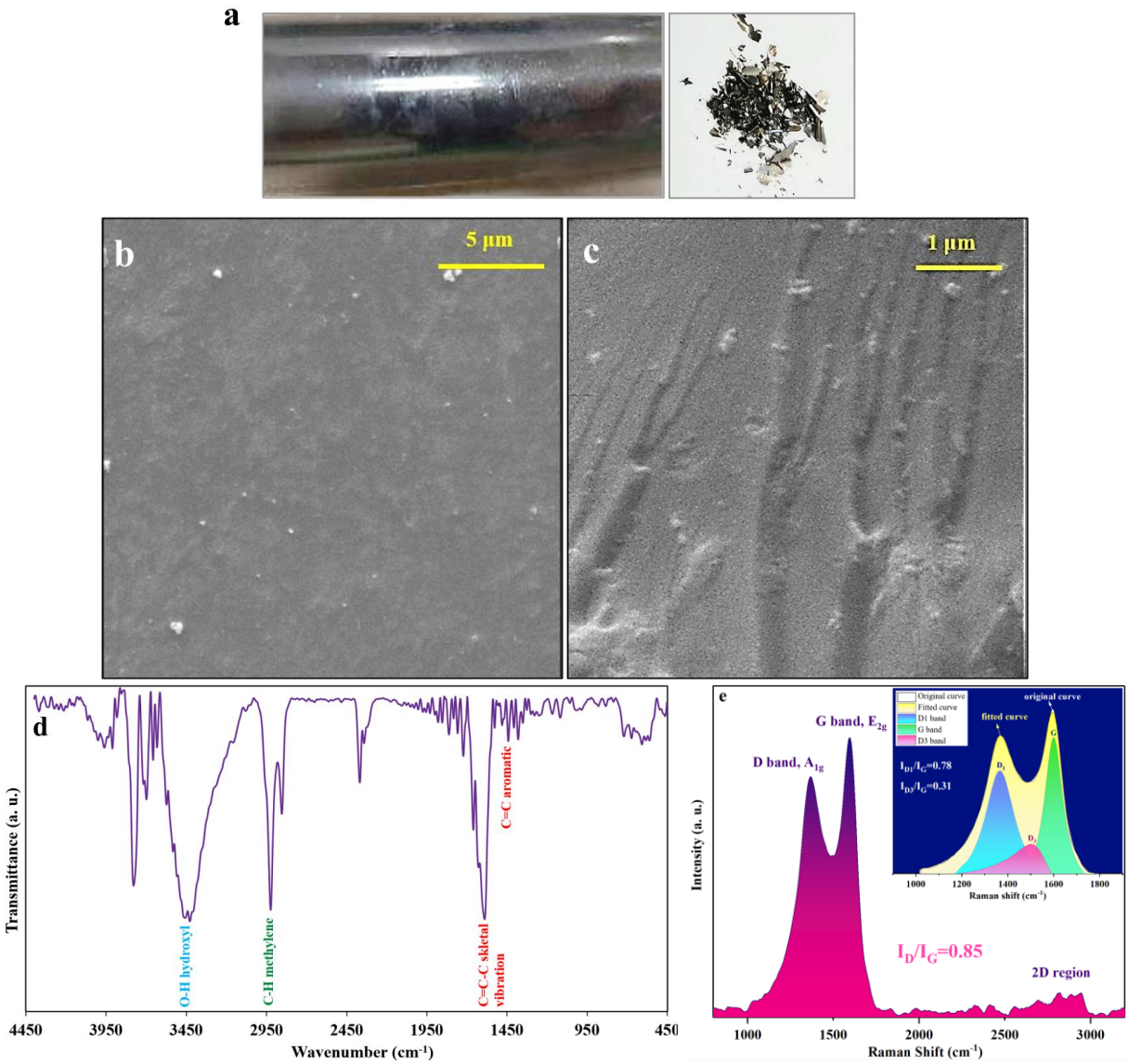

Fig. 1. a) The quartz tube of the tubular furnace in which several low-temperature carbonization of NGr polydivinylbenzene microspheres was conducted. Left: The grayish lustrous coating in a solid state formed along the tube. Right: the carbonaceous matrix separated from the tube and labelled as GCNP. b) SEM image of the coating, showing its uniformity. c) side view of the sample indicating the (layer-by-layer) growth of the coating d) FTIR spectrum of (the) GCNP sample showing the existence of (a) high amount of fused benzene rings as well as aliphatic chains. e) Raman spectrum of GCNP showing the higher G to D intensity ratio (I_D/I_G= 0.87), indicating the high graphitization degree of the (sample. The) inset shows the deconvolution of Raman peaks to precisely indicate the share of crystalline to amorphous part in the sample.

In Fig. 1a left, the quartz tube with a lustrous gray color coating is seen in which nanoporous sulfonated PDVB microspheres were carbonized to 900°C. The coating was easily separated from the tube. In the right photo, the collected sample is shown. Figures 1b and c show SEM images of the GCNP sample. From Fig. 1b it can be seen that the synthesis process has led to the formation of a crack-less and almost uniform coating.

In Fig. 1c, the layer-by-layer formation of the film from the carbonization of nanoporous sulfonated PDVB microspheres is observed. To evaluate the graphitization level of this matrix, it was characterized using Raman and FTIR analysis.

The FTIR spectrum of the GCNP sample is shown in Fig. 1d. The vibration bands in 1380 cm^{-1} are related to the symmetric deformation vibration of methyl umbrella mode, while 1408, 1442 and 1480 cm^{-1} originate from the stretching vibrations of the C=C aromatic bond ring mode [21]. The

[DOI: 10.22068/ijmse.4484]

intense absorption band in 1590 cm^{-1} with shoulders in 1628 and 1660 cm^{-1} arises from the C=C-C skeletal vibration in 6-membered carbon rings with sp^2 hybridization [21, 22]. On the other hand, 2854 and 2924 cm^{-1} are assigned to the symmetric and asymmetric stretching vibrations in methylene chains, respectively [22-24]. Hydroxyl groups due to water adsorption are also identified by the 3424 cm^{-1} vibrational mode as well [25].

Upon heat treatment of sulfonated PDVB during carbonization, due to the bond breaking, benzene ring free radicals along with small aliphatic chains are released [19]. Our previous study confirmed the presence of an intricate xandx hierarchical porous structure in PDVB microspheres consisting of small ink-bottle mesopores and ultramicropores [19]. These pores lead to the local increased pressure due to the confinement of decomposition products inside pores (the) nanoscale spaces. This condition results in action nanopores as nanoreactors to convert benzene free radicals to FBRs. The existence of the C=C-C skeletal vibration sharp band implies that despite the complex pore structure of microspheres that makes the exit egress of nanoreactor products difficult, some FBRs succeed in escaping to the furnace free space and arrive at the carbon coating deposit onto the forming carbon coating.

The Raman spectrum of the sample (Fig. 1e) exhibits two G and D bands in ~ at approximately 1597 cm^{-1} and 1366 cm^{-1}, respectively. The former is assigned to the E_{2g} symmetry related to the sp^2 hybrid in carbon materials. This vibration mode directly reflects the in-plane ordered arrangement of fused 6-membered carbon atoms with a hexagonal shape. On the other hand, the latter, i.e. the D-band arises from the A_{1g} symmetry, the breathing mode of the carbon ring. This mode can only activate at the edges of graphene layers or defective carbon rings [25-27]. However, this two-peak pattern generally consists of more peaks.

The more the ordered the arrangement of carbon rings and crystallite length of graphene layers, the less the intensity of the D to G band ratio. Also, the position of the G-band can determine the stacking of graphene layers. If the number of stacked layers increases, the G-position shifts to lower frequencies [29, 30]. Therefore, the I_D/I_G ratio (and) the G-position should be considered to evaluate the graphitization degree of the material. According to this criterion which was addressed by Ferrari and Robertson [30] (G-position= 1597.917 cm^{-1}, I_D/I_G= 0.85) GCNP is in the Graphite region and is predicted to consist of few stacked graphene layers. Compared to our previous study in which the carbonized sample showed the I_D/I_G= 0.87 an I_D/I_G ratio of 0.87 and (a) G-position of 1587.591 cm^{-1} [19], it is expected that the GCNP sample shows a higher graphitization degree consisting of larger crystallite length and fewer graphene layers on average.

To assess the graphitization degree in more detail, the spectrum was deconvoluted and was found to consist of three peaks at approximately 1365, 1500, and 1599 cm^{-1}, corresponding to the D_1, D_3, and G bands, respectively inset in Fig. 1d. The D_1 band is attributed to carbon atoms near the edges of graphene layers [27], while the D_3 band originates from the amorphous carbon fraction in the material [27, 31, 32]. From the deconvoluted curve, the I_{D_1}/I_G and I_{D_3}/I_G ratios were determined to be 0.78 and 0.31, respectively, indicating that the production pathway favors the synthesis of a low-amorphous, highly crystalline product. However, the in-plane growth of the graphene layers remains limited.

In the absence of any similar studies to the present work directly comparable studies, to the best of our knowledge, a review of catalyst-free CVD investigations however rare we compare our results with the rare reports of catalyst-free CVD, was conducted to evaluate the graphitization degree achieved in this work. Kotbi and co-workers [11] synthesized graphene from ethylene gas by low-pressure plasma followed by flash heating.

Substrates included silicon, quartz, tin oxide, glass and polyamide. In none of these cases, a highly crystalline graphene with an I_D/I_G< 1 ratio of less than 1 was reported. Papale et al. [12] used orange oil gas as a carbon source and conducted a low-pressure plasma-enhanced CVD on a silicon wafer or a quartz substrate. This study also failed to produce graphene layers with an I_D/I_G ratio even close to 1. These comparisons highlight the exceptional nature of achieving such a low intensity ratio in our work.

The XRD pattern of the GCNP sample (Fig. 2) shows a broad peak superimposed on sharp peaks, indicating its composite nature. This pattern is similar to that of the CAR-900 sample in our previous study [19], whereas the presence of sharp peaks at 2θ=26.37°, 41.07° and 44.25° distinguishes it from it. These peaks are related to the d-spacings of 0.337, 2.195 and 2.046 nm, assigned to the

[DOI: 10.22068/ijmse.4484]

crystalline crystallographic planes of (002), (100) and (101) in Graphite-2H (JCPDF card-411487, Table 1), respectively. The interlayer d-spacing of Graphite-2H from (002) crystalline planes in the PDF card is 0.337 nm, which exactly matches that of the present sample.

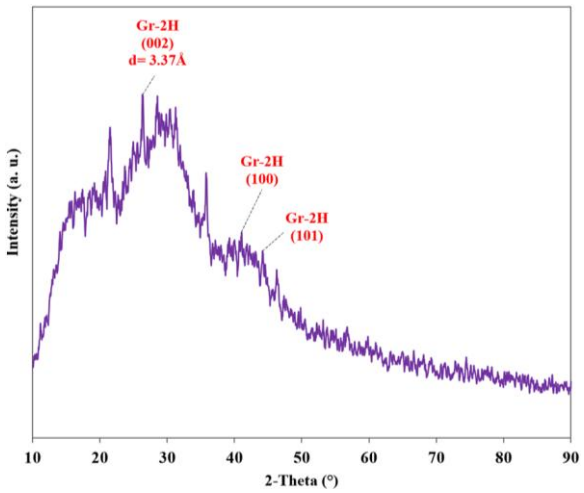

Fig. 2. XRD pattern of GCNP sample representing indicating the composite nature of the material consisting of crystalline and amorphous phases. The inset shows the comparison of the sample peaks with Graphite-2H (PDF 41-1487) which matches to a high extent

Table 1. Comparison between GCNP sample and Graphite-2H (PDF 41-1487) diffraction peaks

GCNP		Graphite-2H (PDF 41-1487)		(hkl)
2θ	d(Å)	2θ	d(Å)	
26.37375	3.37661	26.382	3.37557	002
41.0775	2.19558	42.223	2.13863	100
44.22505	2.04634	44.393	2.03901	101

The degree of graphitization was also calculated from Maring and Marie equation [20] equation (1) and found to be 74% which is a high value for a catalyst/substrate-free carbonization at 900°C. For most carbons prepared at low temperatures, whether or not using catalysts, a two-broad peak pattern is reported, implying an amorphous structure formation in the material [33-35]. The highly crystalline nature of GCNP obtained from XRD analysis is in agreement with Raman results.

The crystallite thickness along the c-axis (L_c) and the basal plane crystallite size along the a-axis (L_a) were calculated by the Scherrer equation from the (002) and (100) peaks, respectively (equations (2) and (3)). The relative value for L_c was obtained as follows: The L_c value was calculated to be ~23 nm, which shows ~69 graphene layers stacked (on) average for this sample, while L_a was calculated to be ~68 nm. The observed discrepancy between the high in-plane crystallite size and relatively moderate stacking order indicates that the process conditions are more conducive to lateral graphene sheet formation than to the alignment of these sheets into stacks. This result proved the Raman result about the formation of graphitic structure with graphene layers of limited in-plane crystallite size.

It should be noted that, due to the low temperature applied during carbonization (900°C), some organic residues are still present (FTIR spectrum, aliphatic groups in 1380, 2854 and 2924 cm^{-1}), which is responsible for the appearance of other sharp peaks in 21.51° and 35.82°, since these peaks are available in JCPDS cards 31-1705, 40-1995, 50-2246, 4-0365, 40-1892, and the like. The appearance of these peaks was also reported by other researchers as well [36-38].

3.2. HRTEM Study of the Sample

To study the GCNP sample in more detail, HRTEM was used to characterize its microstructure. SAED patterns were recorded and FFT images were calculated to determine the crystallographic characteristics of the investigated region as well. HRTEM micrographs and calculated SAED patterns are depicted in Fig. 3.

Fig. 3a shows a region containing several layers and small hexagonal flakes formed alongside it. Surprisingly, in the SAED pattern of this image Fig. 3(b), a significant number of diffraction spots in a hexagonal arrangement which have filled all over the pattern, as well as a few narrow rings are seen. The appearance of too many spots covering the entire pattern in a hexagonal shape implies that there are highly crystalline domains larger than the coherence width of the electron beam. To highlight the exceptionally highly ordered arrangement of the spots in Fig. 3(b), parallel lines with a 60° rotation angle and constant spacing were drawn resulting in the display shown in Fig. 3c. These lines have passed through all spots. Such a full spot diffraction pattern representative of a super high crystallinity has been reported for multilayer graphene [38] and natural graphite so far [39]. In Fig. 3d, the identified crystalline planes (resulting) from solving the hexagonal lattice are (shown).

D-spacings of spots were calculated and displayed in Table 2. Results showed that spots and rings

[DOI: 10.22068/ijmse.4484]

belong to the Graphite-2H (JCPDS card 41-1487) structure which consists of graphene layers with ABAB stacking order. Based on the comparison with the JCPDS card 41-1487 one can find that only one crystalline plane (102) is absent in the SAED pattern of the sample which shows an absolutely highly crystalline nature of the studied area. In addition, this feature has led to the appearance of second, third and even fourth order of crystalline planes spots 11 to 17 in Fig. 3(b) and in Table 2.

After all, the lattice constants of the hexagonal unit cell of the sample which are calculated from (002) and (100) crystalline planes, as well as the comparison with Graphite-2H are listed in Table 3.

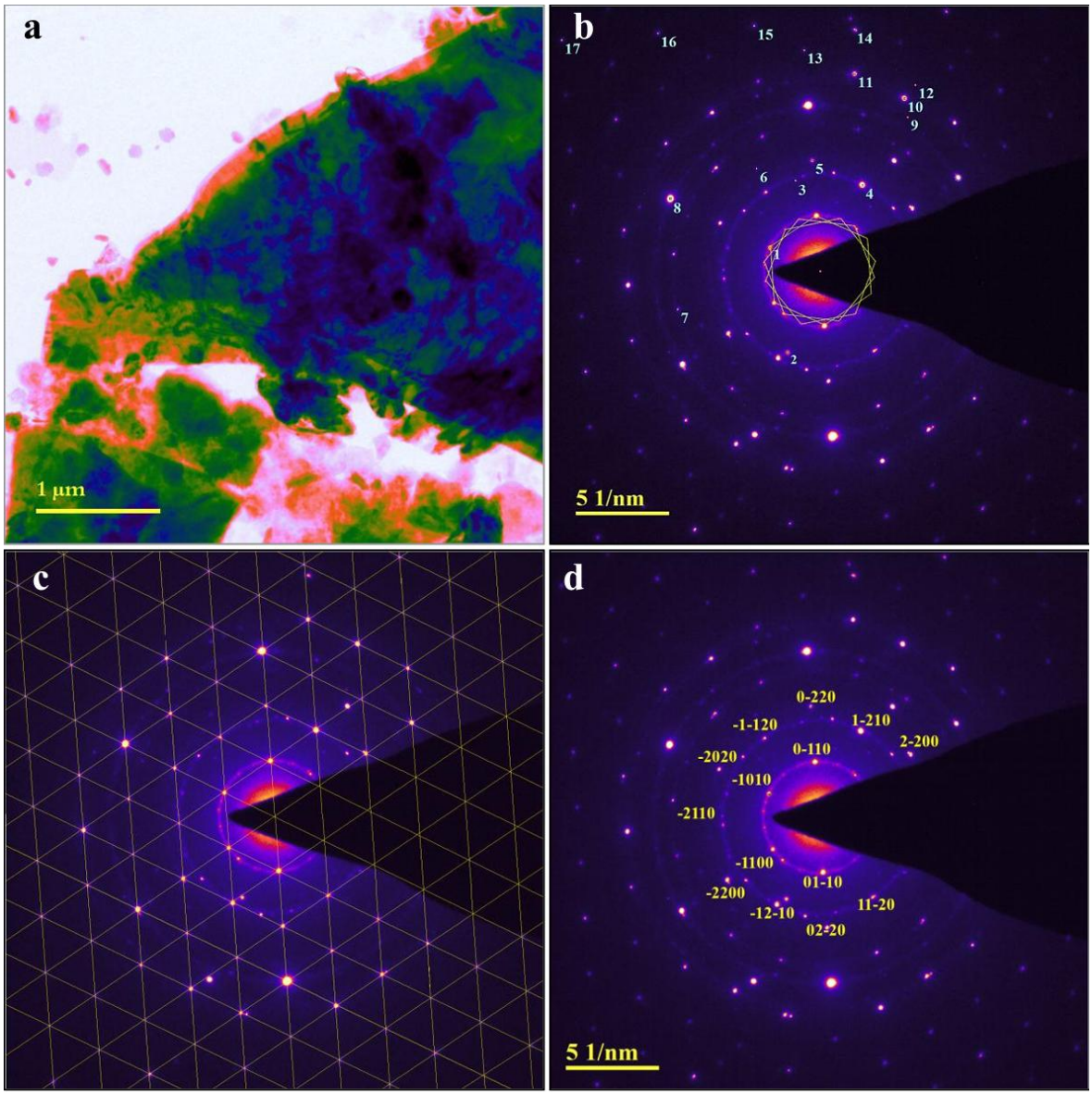

Fig. 3. a) TEM image of GCNP consisting of large multilayer particles besides small hexagonal flakes upper left of the image, restricted in a small rectangular. b) SAED pattern of the TEM image (a), composed of a significant number of diffraction spots covering all the entire pattern and a few narrow circles. This pattern indicates the presence of crystalline areas with large sizes as well as polycrystalline areas. The hexagonal arrangement of spots shows a p6mm symmetry of the crystals. The related crystalline planes according to d-spacings calculated from the radius of spots are presented in Table 2. Three hexagons in the central part of the pattern show the presence of at least three crystalline layers in the studied region. c) The SAED pattern meshed by parallel lines with a 60° angle passing through the spots of the pattern, showing the exceptionally highly ordered structure of the sample. d) The indexed SAED pattern obtained from solving the hexagonal crystal lattice

[DOI: 10.22068/ijmse.4484]

Table 2. Calculated d-spacings in Fig. 3(b) and comparison with Graphite-2H PDF card 41-1487 which resulted in the determination of related crystalline planes. Different green shades represent the (differences in d-spacing in) Graphite-2H and the GCNP sample. (Dark greens indicate the closest values to those on the reference card, while light green indicates) the larger difference between them. Spots 11 to 17 are related to the higher-order reflections of the main d-spacings second, i.e., third and fourth order of main d-spacings in the reference card

Spot	GCNP d-spacing (Å)	Graphite-2H PDF 41-1487 d-spacing (Å)	$\Delta d=d_{Graphite\text{-}2H}-d_{GCNP}$ (Å)	(hkl)
1	3.376	3.37563	0.000370	(002)
2	2.134	2.13865	-0.004650	(100)
3	1.993	2.03901	-0.046010	(101)
4	1.956	2.03901	-0.083010	(101)
5	1.68	1.6811	-0.001100	(004)
6	1.55	1.54777	0.002230	(103)
7	1.269	1.23408	0.034920	(110)
8	1.125	1.12084	0.004160	(006)
9	1.057	1.05672	0.000280	(201)
10	0.9735	0.9924	-0.018900	(114)*
11	0.9343	0.903685	0.030615	(204)
12	0.8947	0.903685	-0.008985	(204)
13	0.8434	0.8439075	-0.000508	(008)
14	0.767	0.773885	-0.006885	(206)
15	0.7367	0.71288333	0.023817	(300)
16	0.65	0.67967	-0.029670	(303)
17	0.5403	0.52836	0.011940	(402)
*This peak is not available in the PDF card 41-1487. It was introduced in ref [40]				

Table 3. Calculated lattice constants for GCNP studied area calculated from data in Table 2

plane	GCNP d-spacing (nm)	Graphite-2H (PDF 41-1487) "a" lattice constant (pm)	Graphite-2H (PDF 41-1487) "c" lattice constant (pm)	GCNP "a" lattice constant (pm)	GCNP "c" lattice constant (pm)
(002)	0.3376	-	675.2	-	675.2
(100)	0.2252	246.9	-	246.4	-

The "a" and "c" lattice constants which are the hexagonal unit cell dimensions were calculated to be 246.4 and 675.2 pm, respectively. In a hexagonal lattice, c is the distance between two A-A layers. On the other hand, a is the distance between two parallel sides of carbon hexagons. These parameters are schematically presented in Fig. 4a and (b).

From Table 3, it is concluded that these parameters are the same as the Graphite-2H unit cell. These data in accordance with data in Table 2 show that the studied region of GCNP in Fig. 3 has crystallized to Graphite-2H structure to a superb high extent. The constructed structure according to the lattice parameters obtained in Table 3 is shown in Fig. 4.

In the following, the results of the HRTEM study of one of the hexagonal flakes in Fig. 3a are presented.

Fig. 5a shows the HRTEM micrograph recorded from hexagonal flakes in Fig. 3a. The highly crystalline particle with a 120° angle as well as a long-range order of small hexagons (is) seen. Further analysis via Fast Fourier Transform (FFT) is shown in the upper-right inset of Fig. 5a, revealing bright spots indicative the structure's high symmetry. The related spot dimensions were calculated and are listed in Table 4. Also, the index pattern is visible in the bottom-right inset.

Considering the graphene lattice and 6-fold carbon rings of the layer one can conclude that the carbon atoms in the studied region are crystallized to a graphene sheet to a very high extent. The restricted area of the sample in Fig. 5a which is illustrated with a yellow rectangle was enlarged to study the arrangement of carbon atoms in more detail (Fig. 5b). From this image, carbon hexagons with a honeycomb structure are obviously seen. Also, the inverse FFT image was established which is shown in Fig. 5c.

[DOI: 10.22068/ijmse.4484]

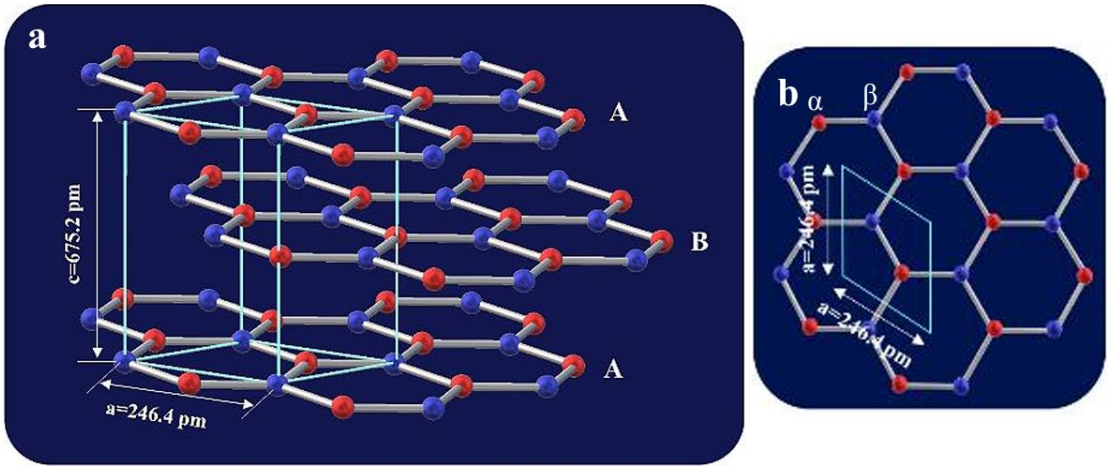

Fig. 4. Constructed structure of graphite-2H according to the calculated lattice constants from SAED pattern a) Side view of the graphite structure with Bernal stacking order ABA. Red and blue spheres represent C atoms in α and β sites of the Graphite basal plane graphene layer. The corresponding unit cell is determined by a light blue rhombohedral prism. Dimensions of the prism are designed according to the lattice constants obtained from calculations of the SAED pattern, presented in Table 3. b) Top view of Graphite basal plane a single graphene layer in which the unit cell is displayed with a light blue rhombic shape. The lattice constant equals the calculated "a" shown in Table 3. The unit cell constants are in excellent agreement with the Graphite-2H unit cell (a lattice constant of Graphite-2H=0.246.9 pm and the c parameter of this structure is 675.2 pm)

These images clearly show the p6mm symmetry of carbon atoms in a graphene layer which resembles multilayer graphene resulting from the CVD process [43, 44]. Remarkably, the dimensions of hexagons that appeared in the micrograph and inverse FFT image are equal to those of hexagons in a graphene sheet Fig. 5b and (c) [44, 45]. To reveal the high crystallinity of the flake, the edge zone was further analyzed at higher magnification.

HRTEM micrographs in Fig. 6 indicate the unambiguously highly crystalline nature of the flakes with higher resolution. To explore the symmetry of the region, an FFT image of Fig. 6a was obtained which is illustrated in the inset. The parameters are the same as Table 4 which is quite equal to the graphene lattice. Micrographs of the studied area in higher resolutions are exhibited in Fig. 6b, c and d wherein carbon atoms with a triangular arrangement are clearly seen. In analogy to graphene and graphite samples in which only β-atoms are visible [42, 46], in the present studied region only 3 atoms from 6 atoms in a 6-fold ring is seen. It is worth noting that in Bernal stacking ordered graphite (ABA sequence), the distance of α-atoms (Fig. 4b) from each other in AA layers equals the doubled amount of β-atoms due to the sliding of the B layer with respect to A layer. This affects the π-π interaction between layers which results in the disappearance of α-atoms in some micrographs. In Fig. 6d, the respective honeycomb structure with only β-atoms is displayed. Also, the line 1 profile of the micrograph was measured which showed the 0.251 nm distance between atoms. This length is equal to "a" lattice constant of graphene sheets [44].

Fig. 7a shows the HRTEM micrograph of another particle in the GCNP sample. The zoomed area of the sample is displayed in the bottom right inset of Fig. 7a for which lattice fringes are obviously observed. No grain boundary or change in growth direction was seen for this large particle, which is close to 1 μm in length, implying the existence of a completely crystalline domain. The FFT pattern of this particle was produced the upper left inset of Fig. 7a. The appearance of an ordered hexagonal arrangement of spots indicates the existence of a highly ordered hexagonal structure of the sample. However, the distance between spots in the central hexagon varies when moving from one spot to another. This stretched hexagon in addition to the presence of other 10 spots in only two quarters of the image, indicates that the crystalline structure of the particle has an anisotropic character. To study the crystalline features of the particle in more detail, the IFFT image of the sample was reconstructed Fig. 7(b). The inset shows the enlarged area of the IFFT image to reveal its characteristics more clearly. The layered structure is easily identified by two lines intersecting the image points, forming a 67.19° angle.

[DOI: 10.22068/ijmse.4484]

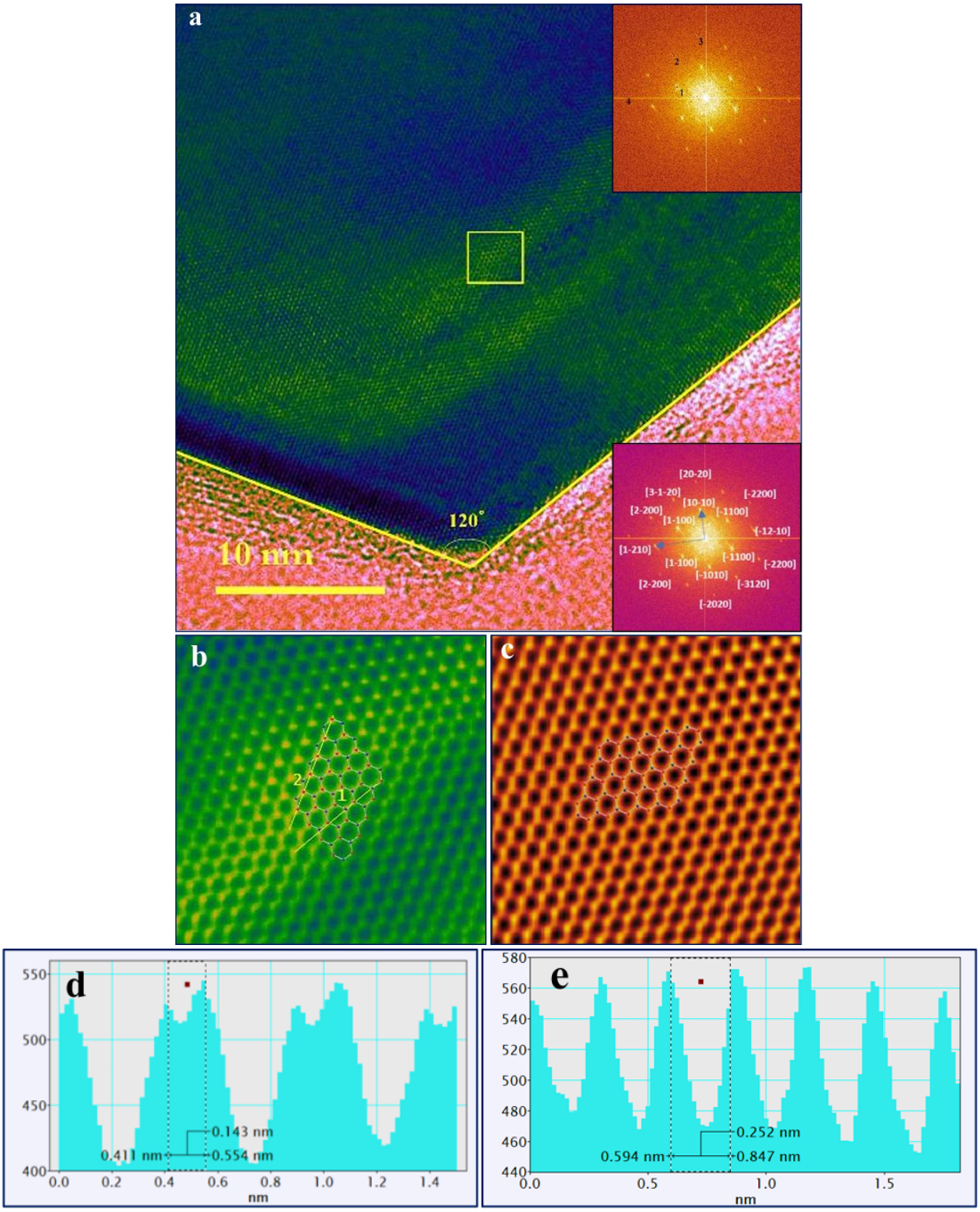

Fig. 5. a) HRTEM image of one of the hexagonal flakes shown in the black rectangle in Fig. 3a showing the high long-range order of 6-fold rings. The upper right inset shows the FFT pattern of the image consisting of large bright spots implying the very highly ordered arrangement of the studied region, resembling CVD-derived multilayer graphene. The respective dimensions of spots are calculated and listed in Table 4. The bottom right inset shows the indexed FFT pattern of the image. b) The enlarged area of the yellow rectangle in the image (a), displays the perfect graphene sheet structure with p6mm symmetry on top of the flake, resembling HOPG. The designed honeycomb structure of the graphene sheet is seen in the image wherein red and blue circles are C-atoms occupied α and β positions (Fig. 4). c) The simulated IFFT image of the studied region in image (b) is formed by masking spots in the FFT pattern inset of image (a), illustrating the excellent hexagonal symmetry of the honeycomb structure in the graphene layer. d) and e) linear profiles of lines 1 and 2 showing the "a" lattice constant of the graphene sheet and C-C distance in 6-membered carbon rings in the graphene layer, respectively. These results show that the studied flake is one of the highly crystalline domains that contributed to the appearance of spots in the SAED pattern

[DOI: 10.22068/ijmse.4484]

Table 4. Dimensions of spots marked on the FFT pattern (Fig. 5b), show excellent compatibility with that of the graphene layer [41, 42] (Fig. 4b)

Spot	Dimension (nm)	Attributed parameter according to graphene layer dimensions
1	0.252	"a" lattice constant
2	0.1454	C-C length in 6-fold carbon ring
3	0.1255	"a/2"
4	0.09543	"3a/8"

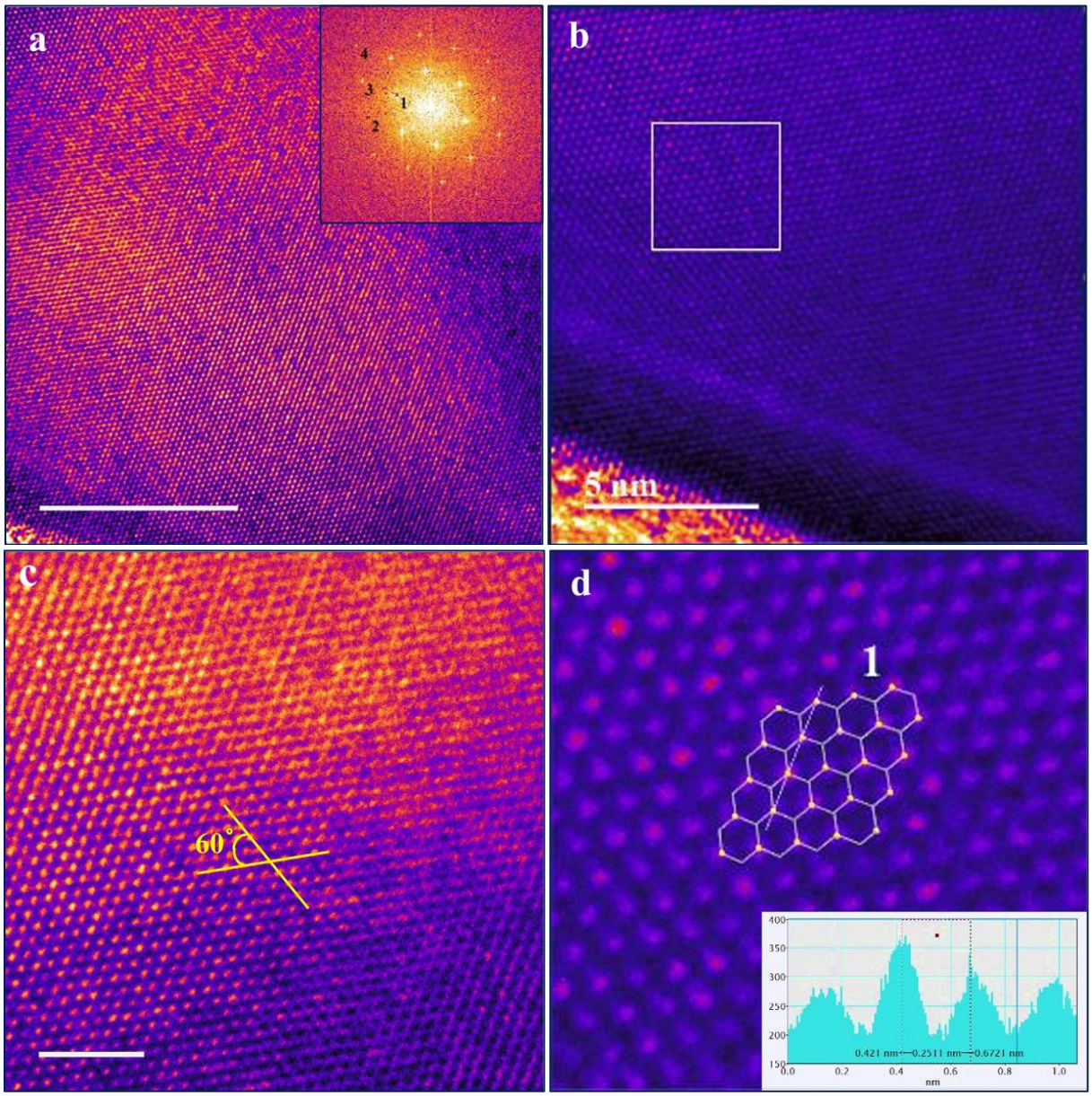

Fig. 6. a) HRTEM image of the edge of crystalline flakes in Fig. 5 showing a corrugation pattern of atoms arrangement. The inset displays the FFT pattern of the region, including 20 bright spots like stars, which show the hexagonal symmetry of the image (a). Parameters were equal to Table 4. b) and c) The edge of the flake with atomic resolution, revealing carbon atoms perfectly arranged in parallel lines with a 60° rotation angle. d) The enlarged area of the white rectangle in the image (a) shows C-atoms (white points) with a triangular arrangement instead of hexagons. These atoms are those carbon atoms that occupied the β-positions displayed in Fig. 4b. Inset is the linear profile of line 1, indicating that C-atoms have a 0.251 nm distance, which is in agreement with "a" lattice of a graphene layer (Fig. 4b).

[DOI: 10.22068/ijmse.4484]

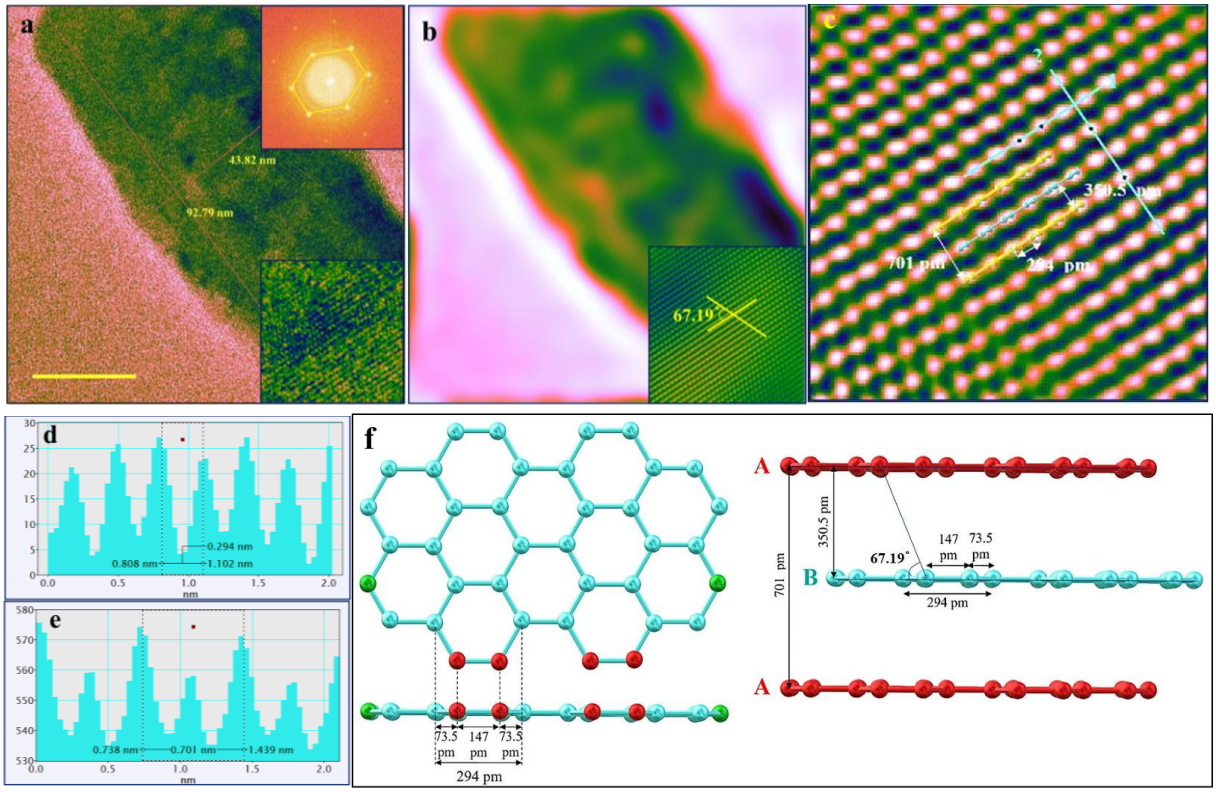

Fig. 7. a) HRTEM micrograph of a particle in the studied region of Fig. 3a. The bottom right inset is the enlarged image of the particle in which lattice fringes are clearly seen. The FFT pattern, the upper left inset, shows large spots which indicate the existence of a highly crystalline zone. However, the stretched hexagon implies the presence of an anisotropic symmetry in the sample. b) The reconstructed inverse FFT image of the HRTEM micrograph was obtained by masking the spots of the FFT pattern to explore the crystalline nature of the sample without disorder. A layered structure comprising stretched points in each layer is clearly visible. The inset shows the enlarged area of the IFFT image with an alternating layered structure. Also, the lines passing through the points form a 67.19° angle, the characteristic angle of lines passing through C atoms in two AB layers (Bernal stacking order. c) The area with further zoom compared to the inset of (b) with the intra-layer point-to-point distance of 0.294 nm and inter-alternate layer d-spacing of 0.701 nm obtained from line profiles (d) and (e), respectively. These parameters are highly compatible with those of Graphite-2H if the side view is exposed to the electron beam (Fig. 4a). Considering three layers in the image, every point is moved forward for one point-to-point distance in the middle layer, while the first and third layers are repeated alternatively so that points are exactly along each other. These features confirm the existence of Bernal stacking order in the sample. The schematic on the image shows the ABA stacking of graphene layers in the Graphite-2H structure which is in accordance with the IFFT image of the sample to a high extent. f) The schematic illustration of Bernal stacking order in Graphite-2H with dimension according to what is measured in (d) and (e) line profiles. This particle is another completely crystalline graphite in the sample

This area was further zoomed in to measure the lattice dimensions more accurately. As it can be observed from Fig. 7c, the particle has a layered structure comprising stretched points, where the distance between them in every layer is 294 pm, while the length of points in alternate layers wherein points are exactly repeating in one direction is 701 pm, according to line profiles in Fig. 7e and d, respectively. These parameters are highly compatible with the distance between the two closest carbon atoms if regarded as one point to its neighbour point in the graphene layer (284 pm) and the “c” lattice constant of Graphite-2H (675.2 pm), respectively. Considering the line’s angle, and inter/intra-layer distances as well as the alternating repetition of points in layers, one can confidently conclude that this particle has a Graphite-2H structure with ABA stacking order which has been exposed to the electron beam from its side cross-section. Based on this conclusion, the stretched points in Fig. 7c are two adjacent carbon atoms with a 73.5 pm distance. On this basis, the Graphite-2H structure

[DOI: 10.22068/ijmse.4484]

of the GCNP sample with p63/mmc symmetry is schematically represented in Fig. 7f.

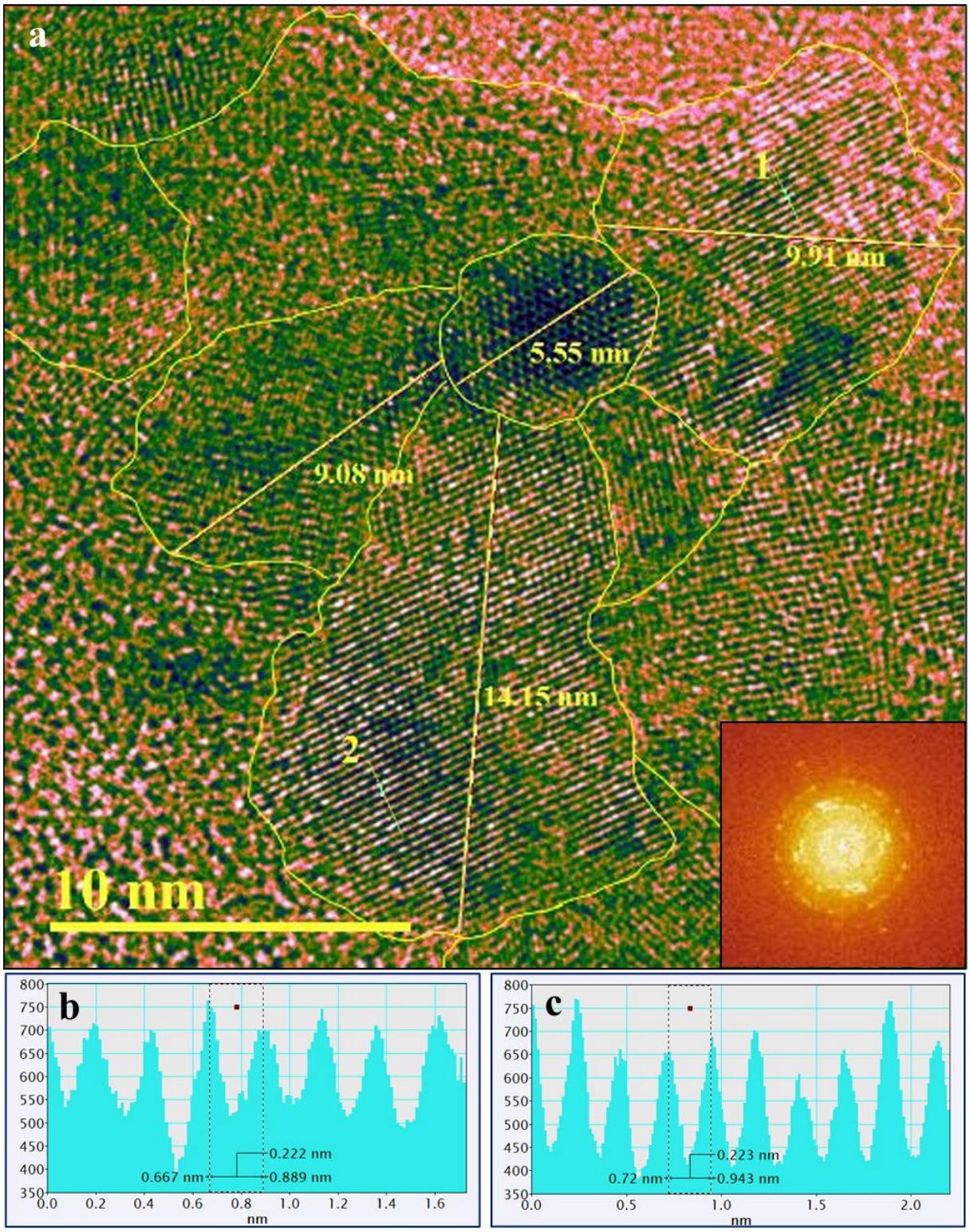

Fig. 8. a) A polycrystalline area of GCNP sample with various growth directions. Some of the grain sizes are shown in the picture. The inset shows an FFT image, indicating the presence of multiple crystalline domains in the studied region. Lattice fringes were measured in randomly selected regions which are displayed in b) and c) d-spacings are related to (100) crystalline plane of Graphite-2H structure according to JCPDS card 41-1487

[DOI: 10.22068/ijmse.4484]

Due to the presence of narrow rings in the SAED pattern of the sample shown in Fig. 3(b), one can deduce that GCNP has polycrystalline areas as well as large crystals. Fig. 8a shows one of these polycrystalline areas of the sample. Various growth directions of grains with different sizes are clearly visible in this picture. To identify the crystalline planes of this area, line profiles (b) and (c) from lines 1 and 2 were recorded, respectively. The measured d-spacing of 0.22 nm indicates that the lattice fringes correspond to the (100) planes of the graphite structure, according to JCPDS card 41-1487. Other regions of the sample were also explored by TEM, whose results are shown in the following.

Fig. 9 shows another region of the GCNP sample explored by TEM. In accordance with the previous region in Fig. 3, this area consists of large crystalline domains and polycrystalline particles spots besides rings in the SAED pattern. However, a diffused circle in the center of the pattern implies the presence of an amorphous phase as well. These results agree with the XRD pattern of the sample shown in Fig. 2. The presence of spots indicates that crystals with large areas relative to the beam are present in the sample. Respective d-spacings were calculated and listed in Table 5.

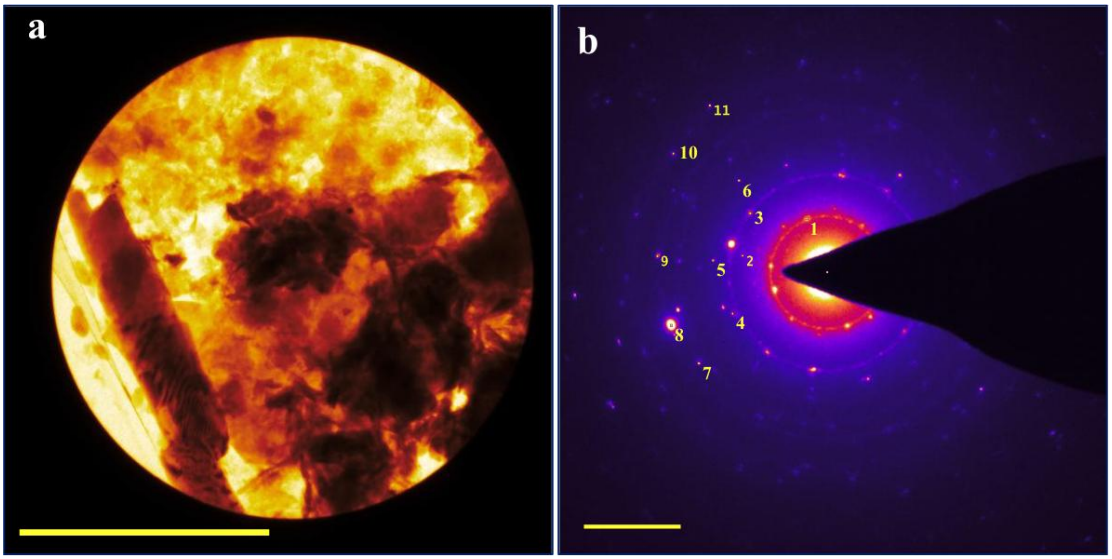

Fig. 9. a) and b) TEM and SAED patterns of another region of the GCNP sample, respectively. The SAED pattern of (a) comprises of spots, narrow ring and a diffused circle in the centre, indicating the composite nature of the area including large crystals, polycrystalline area and amorphous regions, respectively. Crystalline planes attributed to spots and rings are listed in Table 5

Table 5. Calculated d-spacings in Fig. 9(b) and comparison with Graphite-2H PDF card 41-1487, which resulted in the determination of related crystalline planes. Different green shades represent the difference between the calculated d-spacings of Graphite-2H and the GCNP sample. Dark greens indicate the closest values to those on the reference card, while light green indicates the larger difference between them

Spot	GCNP d-spacing (Å)	Graphite-2H PDF 41-1487 d-spacing (Å)	$\Delta d=d_{Graphite\text{-}2H}-d_{GCNP}$ (Å)	(hkl)
1	3.385	3.37563	0.00937	(002)
2	2.241	2.13865	0.10235	(100)
3	1.995	2.03901	-0.04401	(101)
4	1.861	1.8074	0.05363	(102)
5	1.685	1.6811	0.0039	(004)
6	1.52	1.54777	-0.02777	(103)
7	1.226	1.23408	-0.00808	(110)
8	1.171	1.12084	0.01062	(112)
9	1.132	1.05672	0.01116	(006)
10	0.9952	0.9924	-0.02431	(202)
11	0.9481	0.903685	-0.0443	(114)*
*This peak is not available in the PDF card 41-1487. It was introduced in ref [40].				

[DOI: 10.22068/ijmse.4484]

Compared to JCPDS card 41-1487, it is obtained that the sample has a Graphite-2H structure, which consists of graphene layers with a honeycomb structure stacked on each other with an ABA sequence. “A” and “c” unit cell constants were also calculated which results are shown in Table 6.

Comparing lattice constants in this area with those of the previous region (Table 3) as well as SAED patterns of both implies that the explored region in Fig. 3 and 9 are completely crystallized to Graphite-2H structure, but the crystallinity of the area investigated in Fig. 9 is weaker. Data in Table 6 are also consistent with this conclusion. It can be seen that the unit cell dimensions are slightly larger than those in Table 3. This area was further investigated at higher magnifications.

Fig. 10 shows two other regions of the sample in Fig. 9, which were randomly selected. These areas show highly ordered zones that result in spots and a diffused circle in the middle of the FFT patterns, indicating the presence of a disordered area. The corrugated pattern shown in Fig. 10a was simulated to reveal its crystalline part by selecting spots in the FFT image. Fig. 10(b) shows the obtained IFF image, in which the area's highly symmetric nature is evident. The other micrograph (Fig. 10c), with a remarkably higher number of spots in its FFT pattern and a smaller, more diffuse circle the inset compared to Fig. 10a, indicates the higher crystallinity of this domain.

A simulated IFFT image of this area (Fig. 10d) was also produced. To display its high symmetry, the boxed region with the dark blue rectangle was enlarged and shown in Fig. 10e. One can clearly recognise the highly ordered honeycomb structure with stretched vertices and doubled dimensions of the graphene structure in this image. Dimensions were recorded as 506 pm and 270 pm, which are double amounts of “a” lattice constant and C-C distance related to the graphene structure, respectively. The inset shows the reconstructed structure of this area with respect to the basal plane of graphite which unveils the hidden atoms of the structure.

Considering three fused carbon rings containing 13 atoms of carbon, only 6 atoms are easily attributed to the IFFT image. However, by more precisely looking at the reconstructed IFFT image with respect to the schematic structure, one can conclude that the stretched vertices are the result of two adjacent carbon atoms' participation in the FFT pattern. Choosing the 0.142 nm spots from the FFT image inset of Fig.10c, hidden C-atoms were revealed, and the combined stretched vertices were separated so that the perfect basal plane of graphite was obtained (Fig. 10(h) and (i). As can be seen from the line profiles (Fig. 10(j) and (k), lattice constants and C-C distance are in close agreement with the graphene sheet.

3.3. Nanoreactors Network-Directed Graphitization Mechanism

In a typical CVD process for graphene production, a high-purity hydrocarbon gas, hydrogen, a metal catalyst and substrate, and elevated temperatures above 1000°C are employed. The general mechanism involves the decomposition of gas molecules, adsorption of the resulting species on the metal surface, dehydrogenation, and finally the arrangement of atomic carbon into the sp^2-bonded honeycomb lattice on the catalyst [47, 48]. Some studies have reported catalyst-free CVD of graphene on quartz substrates [49, 50]. In these cases, carbon atoms are generated by plasma [49] or by reactive oxygen and hydrogen gases [50], adsorbed on the planar quartz surface, and subsequently organized into a hexagonal sp^2 structure. Although these approaches eliminate the catalyst, they still rely on the decomposition of precursor molecules to atomic carbon, followed by surface-mediated atomic arrangement into graphene layers. In contrast, the present work demonstrates a fundamentally different route. Structural, microstructural, and chemical analyses of the GCNP sample reveal that carbon coatings formed on the inner wall of the quartz furnace tube, by low-temperature carbonization of nanoporous sulfonated PDVB microspheres, are highly graphitized and even contain completely crystalline regions.

Table 6. Calculated lattice constants for GCNP studied area calculated from data in Table 5

plane	GCNP d-spacing (nm)	Graphite-2H (PDF 41-1487) “a” lattice constant (pm)	Graphite-2H (PDF 41-1487) “c” lattice constant (pm)	GCNP “a” lattice constant (pm)	GCNP “c’ lattice constant (pm)
(002)	0.3376	-	675.2	-	677.0
(100)	0.2252	246.9	-	258.8	-

[DOI: 10.22068/ijmse.4484]

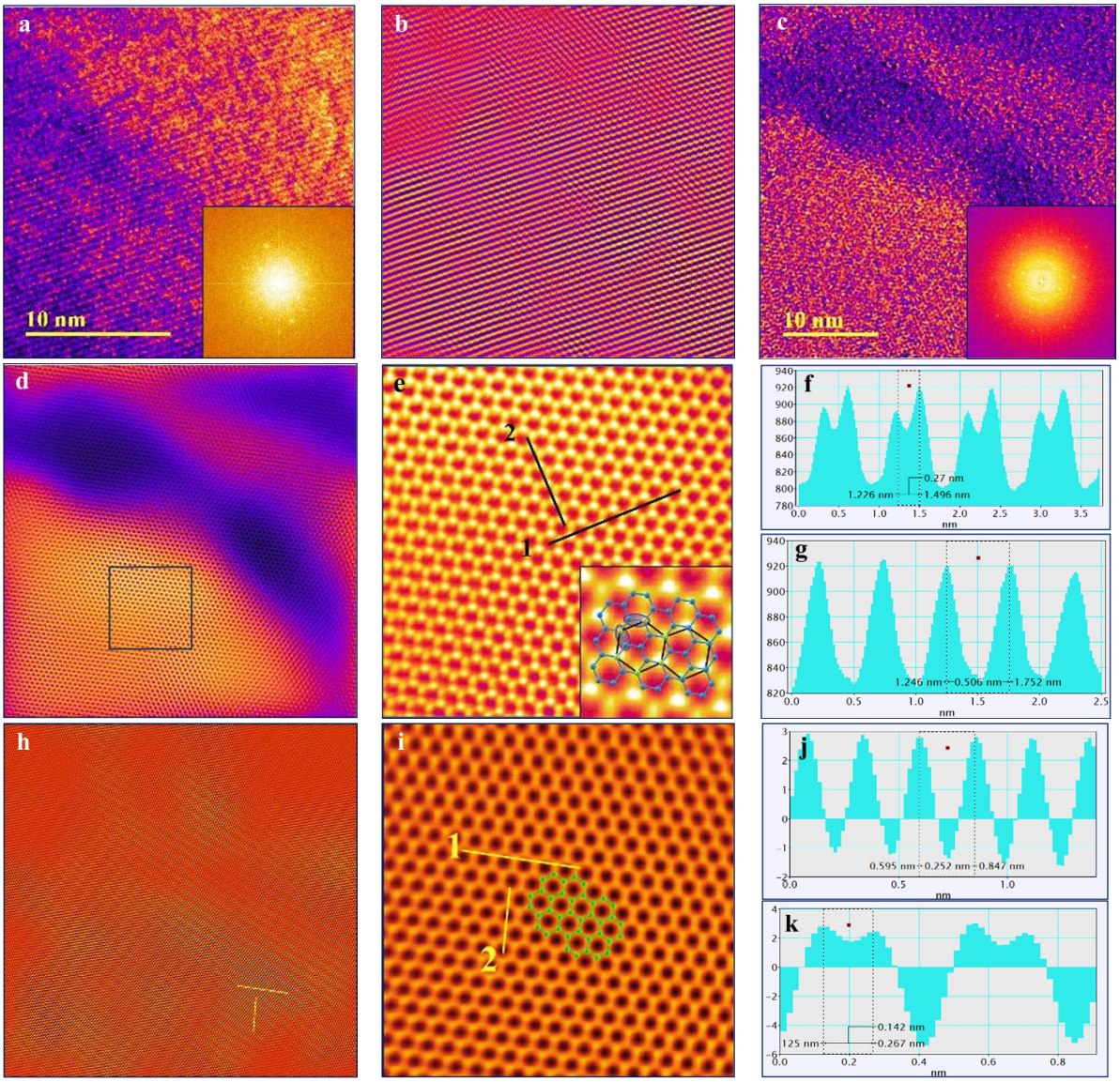

Fig. 10. a) to d) Every row shows HRTEM micrographs (left) of two randomly selected regions of the GCNP sample explored in Fig. 9, as well as its FFT pattern (inset) and simulated IFFT images (right) showing the ordered structure of the sample. e) The enlarged area of the image (d) of the boxed region, illustrating the highly ordered honeycomb structure with doubled dimensions of that of graphene according to the measured line profiles 1 and 2 shown in (f) and (g), respectively. The inset shows the simulated basal-plane structure relative to the IFFT image. Green points are those carbon atoms that are apparently detected in the IFFT pattern. However, the stretched vertices may be the result of the appearance of two adjacent carbon atoms boxed in violet ovals. h) IFFT image of image (c) simulated with 6 spots preferably selected from the FFT pattern displayed in the inset of (c), to unveil the hidden perfect graphene structure, which was not observable by all spots masking of the FFT pattern. The enlarged area is shown in (i). Measured dimensions are the same as graphene, which are displayed in (j) and (k) from lines 1 and 2, respectively

This process is a gas-phase method, yet it occurs without any metal catalyst, substrate, high temperature compared to CVD process or carbonization and graphitization of organic precursors, laser, plasma, or specialized equipment.

The formation mechanism of the GCNP coating differs fundamentally from conventional CVD. Here, the evolved species generated during carbonization of porous NGr microspheres transform extensively into few-layer graphite on the furnace wall. Since no external factor assists in decomposing these groups into atomic carbon, the high degree of graphitization must arise from a mechanism other than atomic-level arrangement. Our previous study

[DOI: 10.22068/ijmse.4484]

showed that sulfonated PDVB microspheres provide nanopores that act as nanoreactors, enabling the fusion of benzene free radicals (FBRs) at temperatures as low as 250°C [19]. The spatial confinement imposed by supermicropores and small ink-bottle mesopores (~95% of the total pore volume) ensures that benzene-derived radicals remain confined and undergo fusion within the pores. However, this same confinement restricts radical growth, limiting graphitization within the microspheres themselves and leaving the potential of the nanopore network unexplored.

In this study, we examine the function of the interconnected nanopore network in facilitating macroscale graphitic film formation. The pore architecture—ink-bottle shaped mesopores and supermicropores linked by narrow molecular-scale necks (~0.6 nm) [19] —drives a pore blocking/ percolation process during pore depletion. As a result, FBRs are not abruptly released into the quartz tube but are delivered (at) a controlled rate. This structure not only constrains the size of moieties exiting through narrow apertures, ensuring the transport of only small, highly active FBRs, but also regulates their release rate due to the network's complexity. Such controlled delivery of precursors into the reaction zone parallels strategies in CVD where deliberate regulation of hydrocarbon feed [51] or spatial confinement near growth surfaces [52-54] leads to enhanced crystallinity. Consequently, the nanopore-guided release mechanism enables the formation of a continuous, highly crystalline graphitic coating on the quartz wall, achieved under conditions far milder than conventional methods.

In Fig. 11, a schematic of an individual ink-bottle nanopore as a nanoreactor for production of FBRs from decomposing pore walls during carbonization as well as pores network are displayed.

Within the large free space of the quartz tube, the released graphitizing moieties—small FBRs—are able to interact and assemble into extended graphitic structures. This growth proceeds laterally through fusion of other FBRs or benzene-derived radicals emerging from the microsphere surface, and vertically via π–π stacking onto already-formed FBRs. Evidence for such lateral growth processes was established in our previous study by FTIR and Raman analyses of microspheres heated from room temperature up to 900°C and 1100°C [19].

Similar observations (have also been) reported by Roberson and co-workers [55] who demonstrated the fusion of polyaromatic hydrocarbons (PAHs, chemically analogous to FBRs) at ~320°C, while Talyzin et al. [56] and Ishii et al. [57] documented oligomerization of PAHs below 600°C. In these cases, thermal energy promotes C–H bond cleavage at PAH edges, enabling polycondensation and the formation of larger aromatic domains.

Taken together, these findings support the Nanoreactors network-directed molecular fusion mechanism, distinct from the atomic arrangement pathway of conventional CVD. This mechanism, enabled by the nanoreactor network, governs the formation of highly crystalline few-layer graphite through four sequential steps:

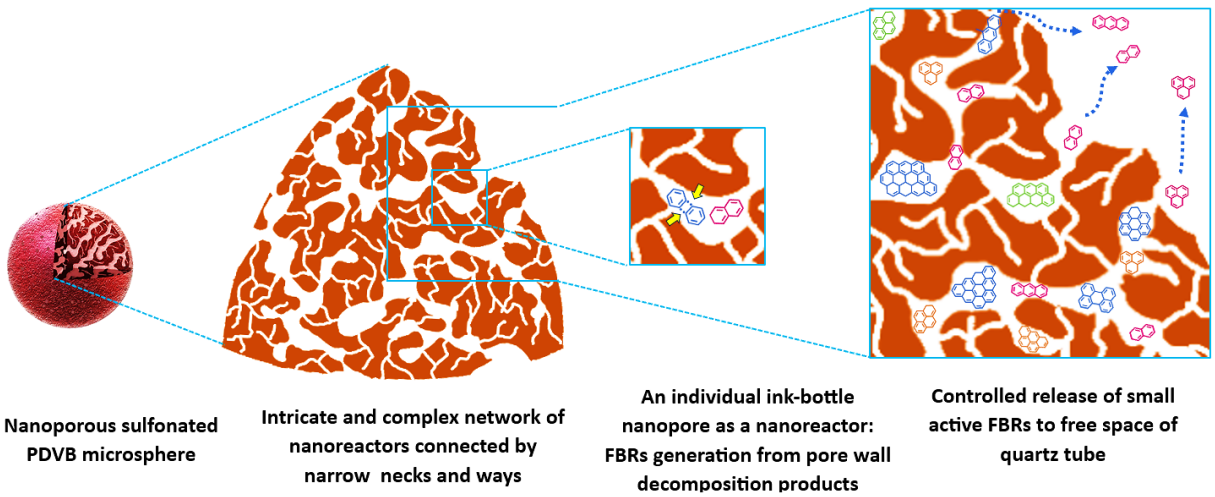

Fig. 11. Ink-bottle nanopores in sulfonated PDVB microstructures and their network connected by narrow necks and ways of molecular size, resulting in the controlled release of small active fused benzene rings to the quartz tube of the furnace and trapping large moieties inside pores

[DOI: 10.22068/ijmse.4484]

i) generation of FBRs within the non-confined spaces of micropores and small mesopores,
ii) classification of FBRs by the pore architecture so that only small, highly reactive moieties escape into the furnace tube,
iii) regulation of the release rate by the complex pore network, and
iv) subsequent lateral growth by in-plane fusion of FBRs and vertical assembly through π–π stacking. Thus, by providing nanoconfined environments to benzene-containing precursors, it becomes possible to enforce their fusion into extended aromatic frameworks, ultimately leading to the growth of graphitic layers. In this pathway, the pore structure itself functions as the critical regulator—synthesizing, filtering, and delivering reactive FBRs into the reaction chamber under controlled conditions. This discovery demonstrates that, independent of extrinsic synthesis parameters such as catalyst, plasma, or high temperature compared to conventional CVD processes, the intrinsic microstructure of the precursor alone can dictate graphitization. Consequently, the present approach represents a paradigm shift in the synthesis of graphitic carbon, offering a low-cost, scalable route toward crystalline graphene and graphite materials for applications in supercapacitors, batteries, and beyond. In Fig. 12, a schematic of the proposed mechanism is illustrated.

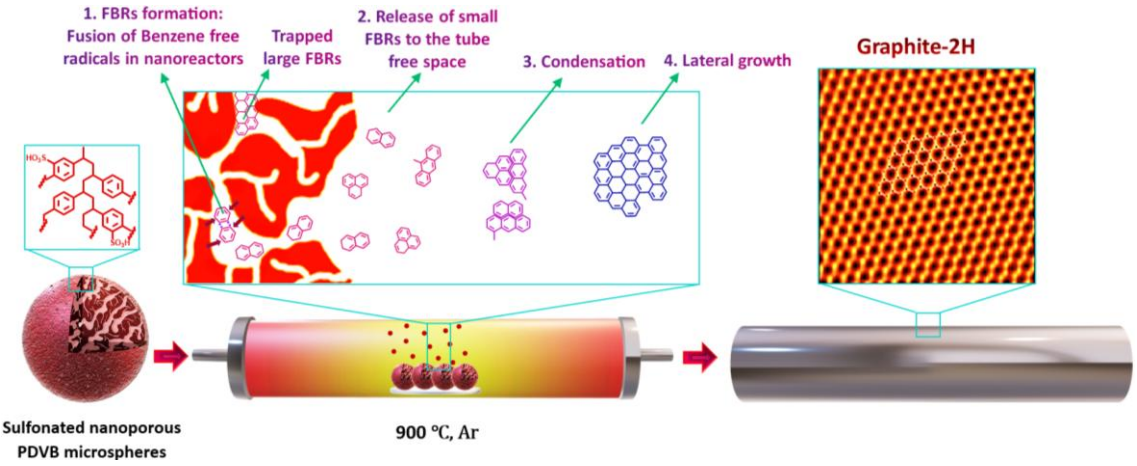

Fig. 12. Schematic for the representation of the nanoreactors network-directed molecular fusion mechanism for the formation of crystalline Graphite-2H from carbonization of sulfonated nanoporous PDVB microspheres

4. CONCLUSIONS

In conclusion, we have demonstrated a simple and scalable catalyst-free route for the synthesis of highly graphitized carbon materials through the direct carbonization of nanoporous sulfonated PDVB microspheres in a conventional tubular furnace. The resulting coatings exhibited an average stack height of 69 layers, a graphitization degree of 74%, and the presence of a well-defined Graphite-2H structure with crystalline p63/mmc domains. This process fundamentally differs from conventional catalyst-free CVD approaches, as no substrate, plasma, laser, or reactive gases are required. Instead, the pore architecture of PDVB microspheres functions as nanoreactors that facilitate (the formation of fusion benzene rings), their classification, and controlled release to the quartz tube free space, wherein lateral growth and stacking lead to ordered graphite layers. Our findings introduce a cost-effective and accessible framework for producing graphene/graphite materials, with tunable potential for multilayer graphene synthesis through adjustment of carbonization cycles and thermal treatment.

ACKNOWLEDGEMENTS

The author wants to acknowledge the Nano-technology Research Center at IUST for its nice contribution to the accomplishment of the polymer microspheres synthesis stage.

REFERENCES

[1] H. Zhao, H. Zuo, J. Wang, and S. Jiao, "Practical application of graphite in lithium-ion batteries: Modification, composite, and sustainable recycling", J. Energy Storage, 2024, 98, 113125, doi: 10.1016/j.est.2024.113125.
[2] D. Zhang, C. Tan, W. Zhang, W. Pan, Q. Wang, and L. Li, "Expanded Graphite-

[DOI: 10.22068/ijmse.4484]

Based Materials for Supercapacitors: A Review", Molecules, 2022, 27, 716, doi: 10.3390/molecules27030716.

[3] D. B. Schuepfer, F. Badaczewski, J. M. Guerra-Castro, D. M. Hofmann, C. Heiliger, B. Smarsly, and P. J. Klar, "Assessing the structural properties of graphitic and non-graphitic carbons by Raman spectroscopy", Carbon N. Y., 2020, 161, 359–372, doi: 10.1016/j.carbon.2019.12.094.

[4] A. Oberlin, "Carbonization and graphitization", Carbon N. Y., 1984, 22, 521–541, doi: 10.1088/0305-4624/5/1/402.

[5] P. J. F. Harris, "Structure of non-graphitising carbons", Int. Mater. Rev., 1997, 42, 206–218, doi: 10.1179/imr.1997.42.5.206.

[6] X. Dou, I. Hasa, D. Saurel, C. Vaalma, L. Wu, D. Buchholz, D. Bresser, S. Komaba, and S. Passerini, "Hard carbons for sodium-ion batteries: Structure, analysis, sustainability, and electrochemistry", Materials Today, 2019, vol. 23, pp. 87-104, doi: 10.1016/j.mattod. 2018.12.040.

[7] R. E. Franklin "Crystallite growth in graphitizing and non-graphitizing carbons", Proc. R. Soc. London. Ser. A. Math. Phys. Sci., 1951, vol. 209, no. 1097, pp. 196–218, doi: 10.1098/rspa.1951.0197.

[8] A. S. Johansson, J. Lu, and J. O. Carlsson, "TEM investigation of CVD graphite on nickel", Thin Solid Films, 1994, 252, 19–25, doi: 10.1016/0040-6090(94)90819-2.

[9] X. Li, W. Cai, J. An, S. Kim, J. Nah, D. Yang, R. Piner, A. Velamakanni, I. Jung, E.Tutuc, S. K. Banerjee, L. Colombo, and R. S. Ruoff, "Large-area synthesis of high-quality and uniform graphene films on copper foils", Science (80-.)., 2009, 324, 1312–1314, doi: 10.1126/science.1171245.

[10] D. X. Luong, K. V. Bets, W. A. Algozeeb, M. G. Stanford, C. Kittrell, W. Chen, R. V. Salvatierra, M. Ren, E. A. McHugh, P. A. Advincula, Z. Wang, M. Bhatt, H. Guo, V. Mancevski, R. Shahsavari, B. I. Yakobson, and J. M. Tour, "Gram-scale bottom-up flash graphene synthesis", Nature, 2020, 577, 647–651, doi: 10.1038/s41586-020-1938-0.

[11] A. Kotbi, M. Lejeune, H. Oughaddou, N. Rajput, X. Zhang, J. Belhadi, Y. Zakaria, D. Richert, F. Piquemal, J. Morán-Meza, M. El Marssi, and M. Jouiad, "Eco-Friendly Deposition of Catalyst-Free Graphene on Diverse Substrates", Adv. Sustain. Syst., 2025, 2500105, doi: 10.1002/adsu.202500105.

[12] L. Papale, B. Philippa, B. Makarenko, O. K. Varghese, and M. V. Jacob, "Sustainable low temperature carrier gas-free growth of graphene on non-catalytic substrates", RSC Sustain., 2024, 2, 995–1002, doi: 10.1039/d3su00417a.

[13] L. Liu, W. Li, Z. Li, F. He, and H. Lv, "Metal-Free Catalytic Preparation of Graphene Films on a Silicon Surface Using CO as a Carbon Source in Chemical Vapor Deposition", Coatings, 2023, 13, doi: 10.3390/coatings 13061052.

[14] Z. Liu, Y. Zeng, Q. Tang, A. Hu, K. Xiao, S. Zhang, W. Deng, B. Fan, Y. Zhu, and X/ Chen, "Potassium vapor assisted preparation of highly graphitized hierarchical porous carbon for high rate performance supercapacitors", J. Power Sources, 2017, 361, 70–79, doi: 10.1016/j.jpowsour.2017.06.058.

[15] H. D. Asfaw,R. Younesi, M. Valvo, J. Maibach, J. Ångström, C. Wai Tai, Z. Bacsik, M. Sahlberg, L. Nyholm, and K. Edström, "Boosting the thermal stability of emulsion–templated polymers via sulfonation: an efficient synthetic route to hierarchically porous carbon foams", ChemistrySelect, 2016, 1, 784–792, doi: 10.1002/slct.201600139.

[16] R. Luo, Z. Wan, P. Mei, Z. Xie, D. Shi, and Y. Yang, "Cross-linked copolymer-derived nitrogen-doped hierarchical porous carbon with high-performance lithium storage capability", Mater. Adv., 2022, 6636–6642, doi: 10.1039/d2ma00310d.

[17] Y. Kawai and T. Yamamoto, "Synthesis of porous carbon hollow particles maintaining their structure using hyper-cross-linked Poly(St-DVB) hollow particles", Adv. Powder Technol., 2020, 31, 614–620, doi: 10.1016/j.apt.2019.11.016.

[18] N. Wang, Y. Yao, L. He, Y. Chen, and B. Sun, "One-step carbonization of poly(styrene/ divinylbenzene) to fabricate N-doped porous carbon for high-performance supercapacitor electrode", J. Porous Mater., 2020, 27, 627–635, , doi: 10.1007/s10934-020-00874-4.

[19] A. Afzalalghom, A. Beitollahi, S. M. Mirkazemi, M. Maleki, and H. Sarpoolaky, "Intervention-Free Graphitization of Carbon Microspheres from a Non-Graphitizing Polymer at Low Temperature: Nanopores

[DOI: 10.22068/ijmse.4484]

as Dynamic Nanoreactors", Small, 2024, 20, 2308082, doi: 10.1002/smll.202308082.
[20] S. Li, W.-L. Song, X. Han, Q. Cui, Y. Zhu, and S. Jiao, "Low-temperature graphitization of lignin via Co-assisted electrolysis in molten salt", Green Energy Environ., 2024, 9, 1449–1458, doi: 10.1016/j.gee.2023.04.006.
[21] M. Asemani and A. R. Rabbani, "Detailed FTIR spectroscopy characterization of crude oil extracted asphaltenes: Curve resolve of overlapping bands", J. Pet. Sci. Eng., 2019. 185, 106618, 2020, doi: 10.1016/j.petrol. 2019.106618.
[22] V. Brusko, A. Khannanov, A. Rakhmatullin, and A. M. Dimiev, "Unraveling the infrared spectrum of graphene oxide", Carbon N. Y., 2024, 229, 119507, doi: 10.1016/j.carbon. 2024.119507.
[23] A. B. D. Nandiyanto, R. Oktiani, and R. Ragadhita, "How to read and interpret ftir spectroscope of organic material", Indones. J. Sci. Technol., 2019, 4, 97–118, doi: 10. 17509/ijost.v4i1.15806.
[24] A. C. S. Talari, M. A. G. Martinez, Z. Movasaghi, S. Rehman, and I. U. Rehman, "Advances in Fourier transform infrared (FTIR) spectroscopy of biological tissues", Appl. Spectrosc. Rev., 2017, 52, 456–506, doi: 10.1080/05704928.2016.1230863.
[25] L. G. Wade, Jr., "Infrared Spectroscopy (IR) Theory and Interpretation of IR spectra presentation", Org. Chem., 2003, 5th, 853–866.
[26] A. C. Ferrari, "Raman spectroscopy of graphene and graphite: Disorder, electron-phonon coupling, doping and nonadiabatic effects", Solid State Commun., 2007, 143, 47–57, doi: 10.1016/j.ssc.2007.03.052.
[27] A. Sadezky, H. Muckenhuber, H. Grothe, R. Niessner, and U. Pöschl, "Raman micro-spectroscopy of soot and related carbonaceous materials: Spectral analysis and structural information", Carbon N. Y., 2005, 43, 731–1742, doi: 10.1016/j.carbon.2005.02.018.
[28] S. Reich and C. Thomsen, "Raman spectroscopy of graphite", Philos. Trans. R. Soc. A Math. Phys. Eng. Sci., 2004, 362, 2271–2288, doi: 10.1098/rsta.2004.1454.
[29] A. C. Ferrari, and J. robertson, "Raman spectrum of graphene and graphene layers", Phys. Rev. Lett., 2006, 97, 1–4, doi: 10.1103/ PhysRevLett.97.187401.
[30] A. C. Ferrari, and J. robertson "Interpretation of Raman spectra of disordered and amorphous carbon", Phys. Rev. B-, 2000, 61, 95–107, doi: 10.1007/BF02543692.
[31] P. A. Goodman, H. Li, Y. Gao, Y. F. Lu, J. D. Stenger-Smith, and J. Redepenning, "Preparation and characterization of high surface area, high porosity carbon monoliths from pyrolyzed bovine bone and their performance as supercapacitor electrodes", Carbon N. Y., 2013, 55, 291–298, doi: 10.1016/j.carbon.2012.12.066.
[32] D. Schmidt, S. Schöner, M. K. Steinhoff, R. Schierholz, K. Steinhauer, D. T. Daniel, S. Speer, A. Kretzschmar, F. Jeschull, A. Windmüller, C.-Long Tsai, H. Tempel, S. Yu, and R. A. Eichel "Impact of Carbonization Temperature on the Structure and Li Deposition Behavior of 3D Dual Metal Carbon Fibers", Small Struct., 2024, 2400311, doi: 10.1002/ sstr.202400311.
[33] L. Xie, C. Tang, Z. Bi, M. Song, Y. Fan, C. Yan, X. Li, F. Su, Q. Zhang, and C. Chen, "Hard Carbon Anodes for Next-Generation Li-Ion Batteries: Review and Perspective", Adv. Energy Mater., 2021, 11, 1–22, doi: 10.1002/aenm.202101650.
[34] Z. Bai, Bi. Zhao, J. Deng, Y. Ren, Y. Li, R.g Wang, F. Zeng, X. Guo, and R. Zhang, "Light-weight and high-efficiency electro-magnetic wave shielding properties based on waste straw porous carbon", J. Mater. Sci. Mater. Electron., 2020, 31, 4963–4971, doi: 10.1007/s10854-020-03063-w.
[35] Y. M. Wang and C. H. Zhang, "Study on Structural Evolution of Synthetic Graphite Derived from Lignite Prepared by High Temperature–High Pressure Method", Crystals, 2022, 12, doi: 10.3390/cryst12040464.
[36] J. Meng, S. Li, and J. Niu, "Crystallite Structure Characteristics and Its Influence on Methane Adsorption for Different Rank Coals", ACS Omega, 2019, 4, 20762–20772, Dec., doi: 10.1021/acsomega.9b03165.
[37] J. Jiang, W. Yang, Y. Cheng, Z. Liu, Q. Zhang, and K. Zhao, "Molecular structure characterization of middle-high rank coal via XRD, Raman and FTIR spectroscopy: Implications for coalification", Fuel, 2019, 239, 559–572, doi: 10.1016/j.fuel.2018.11.057.
[38] A. Mohapatra, M. S. R. Rao, and M. Jaiswal, "Thermal transport in turbostratic multilayer graphene", Carbon N. Y., 2022, [Online].

[DOI: 10.22068/ijmse.4484]

Available: https://api.semanticscholar.org/CorpusID:252083298

[39] L. Yuan, Q. Liu, J. P. Mathews, H. Zhang, and Y. Wu, "Quantifying the Structural Transitions of Chinese Coal to Coal-Derived Natural Graphite by XRD, Raman Spectroscopy, and HRTEM Image Analyses", Energy and Fuels, 2021, 35, 2335–2346, doi: 10.1021/acs.energyfuels.0c04019.

[40] J. Y. Howe, C. J. Rawn, L. E. Jones, and H. Ow, "Improved crystallographic data for graphite", Powder Diffr., 2003, 18, 150–154, doi: 10.1154/1.1536926.

[41] C. B. Clemons, M. W. Roberts, J. P. Wilber, G. W. Young, A. Buldum, and D. D. Quinn, "Continuum plate theory and atomistic modeling to find the flexural rigidity of a graphene sheet interacting with a substrate", J. Nanotechnol., 2010, doi: 10.1155/2010/868492.

[42] S. Hembacher, F. J. Giessibl, J. Mannhart, and C. F. Quate, "Revealing the hidden atom in graphite by low-temperature atomic force microscopy", Proc. Natl. Acad. Sci. U. S. A., 2003, 100, 12539–12542, doi: 10.1073/pnas.2134173100.

[43] H. A. Calderon, C. Kisielowski, P. Specht, B. Barton, F. Godinez-Salomon, and O. Solorza-Feria, "Maintaining the genuine structure of 2D materials and catalytic nanoparticles at atomic resolution", Micron, 2015, 68, 164–175, doi: 10.1016/j.micron.2014.08.007.

[44] R. Y. N. Gengler, K. Spyrou, and P. Rudolf, "A roadmap to high quality chemically prepared Graphene", J. Phys. D. Appl. Phys., 2010, 43, doi: 10.1088/0022-3727/43/37/374015.

[45] B. Luo, B. Chen, A. Wang, D. Geng, J. Xu, H. Wang, Z. Zhang, L. Peng, Z. Xu, and G. Yu, "Chemical vapor deposition of bilayer graphene with layer-resolved growth through dynamic pressure control", J. Mater. Chem. C, 2016, 4, 7464–7471, doi: 10.1039/c6tc02339h.

[46] A. Georgi, P. Nemes-Incze, R. Carrillo-Bastos, D. Faria, S. V. Kusminskiy, D. Zhai, M. Schneider, D. Subramaniam, T. Mashoff, N. M. Freitag, M. Liebmann, M. Pratzer, L. Wirtz, C. R. Woods, R. V. Gorbachev, Y. Cao, K. S. Novoselov, N. Sandler, and M. Morgenstern., "Tuning the Pseudospin Polarization of Graphene by a Pseudomagnetic Field", Nano Lett., 2017, 17, 2240–2245, doi: 10.1021/acs.nanolett.6b04870.

[47] L. Wang, R. Lai, L. Zhang, M. Zeng, and L. Fu, "In Situ Investigating the Mechanism of Graphene Growth by Chemical Vapor Deposition", ACS Mater. Lett., 2022, 4, 528–540, doi: 10.1021/acsmaterialslett.1c00783.

[48] C. M. Seah, S. P. Chai, and A. R. Mohamed, "Mechanisms of graphene growth by chemical vapour deposition on transition metals", Carbon N. Y., 2014, 70, 1–21, doi: 10.1016/j.carbon.2013.12.073.

[49] R. Vishwakarma, R. Zhu, A. A. Abuelwafa, Y. Mabuchi, S. Adhikari, S. Ichimura, T. Soga, and M. Umeno, "Direct Synthesis of Large-Area Graphene on Insulating Substrates at Low Temperature using Microwave Plasma CVD", ACS Omega, 2019, 4, 11263–11270, doi: 10.1021/acsomega.9b00988.

[50] J. Chen, Y. Wen, Y. Guo, B. Wu, L. Huang, Y. Xue, D. Geng, D. Wang, G. Yu, and Y. Liu, "Oxygen-aided synthesis of polycrystalline graphene on silicon dioxide substrates", J. Am. Chem. Soc., 2011, 133, 17548–17551, doi: 10.1021/ja2063633.

[51] S. Bhaviripudi, X. Jia, M. S. Dresselhaus, and J. Kong, "Role of kinetic factors in chemical vapor deposition synthesis of uniform large area graphene using copper catalyst", Nano Lett., 2010, 10, 4128–4133, doi: 10.1021/nl102355e.

[52] Y. Zhang, L. Zhang, P. Kim, M. Ge, Z. Li, and C. Zhou, "Vapor Trapping Growth of Single-Crystalline Graphene Flowers: Synthesis, Morphology, and Electronic Properties", Nano Lett., 2012, 12.

[53] C. Wang, W. Chen, C. Han, G. Wang, B. Tang, C. Tang, Y. Wang, W. Zou, W. Chen, X-A. Zhang, S. Qin, S. Chang, and L. Wang., "Growth of millimeter-size single crystal graphene on Cu foils by circumfluence chemical vapor deposition", Sci. Rep., 2014, 4, 1–5, doi: 10.1038/srep04537.

[54] C. C. Chen, C. J. Kuo, C. D. Liao, C. F. Chang, C. A. Tseng, C. R. Liu, and Y. T. Chen, "Growth of Large-Area Graphene Single Crystals in Confined Reaction Space with Diffusion-Driven Chemical Vapor Deposition", Chem. Mater., 2015, 27, 6249–6258, doi: 10.1021/acs.chemmater.5b01430.

[DOI: 10.22068/ijmse.4484]

[55] L. B. Roberson, J. Kowalik, L. M. Tolbert, C. Kloc, R. Zeis, X. Chi, R. Fleming, and C. Wilkins., "Pentacene disproportionation during sublimation for field-effect transistors", J. Am. Chem. Soc., 2005, 127, 3069–3075, doi: 10.1021/ja044586r.

[56] A. V. Talyzin, S. M. Luzan, K. Leifer, S. Akhtar, J. Fetzer, F. Cataldo, Y. O. Tsybin, C. W. Tai, A. Dzwilewski, and E. Moons, "Coronene fusion by heat treatment: Road to nanographenes", J. Phys. Chem. C, 2011, 115, 13207–13214, doi: 10.1021/jp2028627.

[57] Y. Ishii, H. Song, H. Kato, M. Takatori, and S. Kawasaki, "Facile bottom-up synthesis of graphene nanofragments and nanoribbons by thermal polymerization of pentacenes," Nanoscale, 2012, 4, 6553, doi: 10.1039/c2nr31893h.

[DOI: 10.22068/ijmse.4484]